Article

Emission Control from Transition Metal Dichalcogenide Monolayers by Aggregation-Induced Molecular Rotors

Mike Tebyetekerwa, Yanhua Cheng, Jian Zhang, Weili Li, Hongkun Li, Guru Prakash Neupane, Bowen Wang, Thien N. Truong, Chuanxiao Xiao, Mowafak M. Al-Jassim, Zongyou Yin, Yuerui Lu, Daniel MacDonald, and Hieu T Nguyen

ACS Nano, **Just Accepted Manuscript** • DOI: 10.1021/acsnano.0c03086 • Publication Date (Web): 13 May 2020

Emission Control from Transition Metal Dichalcogenide Monolayers by Aggregation-Induced Molecular Rotors

Mike Tebyetekerwa[1], Yanhua Cheng[2], Jian Zhang[1], Weili Li[3], Hongkun Li[4], Guru Prakash Neupane[1], Bowen Wang[1], Thien N. Truong[1], Chuanxiao Xiao[5], Mowafak M. Al-Jassim[5], Zongyou Yin[6], Yuerui Lu[1], Daniel Macdonald[1] and Hieu T. Nguyen[1]**

[1]Research School of Electrical, Energy and Materials Engineering, College of Engineering and Computer Science, The Australian National University, Canberra, ACT 2601, Australia

[2]State Key Laboratory for Modification of Chemical Fibers and Polymer Materials, College of Materials Science and Engineering, Donghua University, Shanghai 201620, P. R. China

[3]School of Material Science and Engineering & National Demonstration Center for Experimental Materials Science and Engineering Education, Jiangsu University of Science and Technology, Zhenjiang 212003, P. R. China

[4]State and Local Joint Engineering Laboratory for Novel Functional Polymeric Materials, Laboratory of Advanced Optoelectronic Materials, College of Chemistry, Chemical Engineering and Materials Science, Soochow University, Suzhou 215123, P. R. China

[5]National Renewable Energy Laboratory, Golden, CO 80401, USA

[6]Research School of Chemistry, College of Science, The Australian National University, Canberra, ACT 2601, Australia.

ABSTRACT

Organic-inorganic (O-I) heterostructures, consisting of atomically thin inorganic semiconductors and organic molecules, present synergistic and enhanced optoelectronic properties with a high tunability. Here, we develop a class of air-stable vertical O-I heterostructures comprising of a monolayer of transition metal dichalcogenides (TMDs), including WS_2, WSe_2 and $MoSe_2$, on top of tetraphenylethylene (TPE) core-based aggregation-induced emission (AIE) molecular rotors. The created O-I heterostructures yields a photoluminescence (PL) enhancement of up to ~950%, ~500% and ~330% in the top monolayer WS_2, $MoSe_2$ and WSe_2 as compared to PL in their pristine monolayers, respectively. The strong PL enhancement is mainly attributed to the efficient photo-generated carrier process in the AIE luminogens (courtesy of their restricted intermolecular motions in the solid state) and the charge transfer process in the created type-I O-I heterostructures. Moreover, we observe an improvement in photovoltaic properties of the TMDs in the heterostructures including the quasi-Fermi level splitting, minority carrier lifetime and light absorption. This work presents an inspiring example of combining stable, highly luminescent AIE-based molecules, with rich photochemistry and versatile applications, with atomically thin inorganic semiconductors for multifunctional and efficient optoelectronic devices.

KEYWORDS: monolayer semiconductors; photoluminescence pumping; aggregation-induced emission (AIE); molecular rotors; transition metal dichalcogenides; organic-inorganic heterostructures.

Amongst the widely researched two-dimensional (2D) monolayer semiconductors, transition metal dichalcogenides (TMDs) have received enormous attention[1] owing to their optical and electronic properties such as sizeable bandgaps,[2, 3] transitions from indirect bandgaps in bulk materials to direct bandgaps in monolayers,[4, 5] valley polarization possibilities[6, 7] and many others.[8, 9] Their monolayers avail properties such as flexibility and lightweight (due to their thickness of < 1 nm),[10, 11] and quantum-confinement effects which improve their absorption efficiency.[12] More still, recently, van der Waals (vdW) heterostructures of monolayer TMDs have been reported to demonstrate different optoelectronic properties depending on the nature of their moiré superlattices.[13, 14] It is, therefore, possible to build various vertical vdW heterostructures with different properties for a wide range of optoelectronic devices such as solar cells, photodetectors, light-emitting diodes (LEDs) and many others.[10, 15-18] However, under illumination, TMD monolayers tend to have low excitonic photoluminescence (PL) efficiencies due to their high densities of native defect states and formation of multi-quasi particles such as trions and biexcitons favoring non-radiative recombination pathways.[19, 20] Therefore, finding ways to enhance their excitonic PL signal is of great interest to the community.[20, 21]

2D TMD semiconductors interfacing with organic materials show significant improvements in their light-matter interaction properties, resulting in efficient heterostructures for various optoelectronic applications.[22, 23] Previously the carrier dynamics and optical responses of atomically-thin 2D TMDs with organic species such as pentacene,[24-26] tetracene,[27] perylene tetracarboxylic dianhydride (PTCDA),[28] rubrene,[29] and others[23, 30, 31] have been studied. It was found that the created organic-inorganic (O-I) heterostructures demonstrated exciting optoelectronic properties which were sensitive to both the organic molecules' aggregation and arrangements.[23, 31, 32] With the presence of organic species interfacing TMDs, it is possible to

realize various band alignments ranging from type-I, type-II to type-III depending on the materials making up the heterostructure and also to treat some native defects within the TMDs.[23, 33] O-I type-I band alignment is important for organic-TMD heterostructures because they enable an efficient PL pumping, courtesy of charge transfer processes between the O-I heterostructure interfaces.[24] However, to obtain high-quality organic species capable of improving the PL emission of TMDs configured in such heterostructures is not a straightforward approach. The previously reported organic species suffer from their low PL quantum yield, poor stability in air, hardly tunable optical properties, low functionality and poor photophysical chemistry. [24-29]

In this line, an organic material which can overcome the mentioned limitations is highly desirable. Fluorescent aggregation-induced emission (AIE) molecular rotors with twisted intra molecular-charge-transfer properties[34-36] are promising candidates. The nature and configuration of the intramolecular motions in AIE luminogens determine their photophysical energy dissipation pathways.[37] Subsequently, the restriction of these motions amongst the rotors can promote an extraordinary PL emission in these materials at solid state.[38-40] Such a phenomenon is opposite to an aggregation-caused quenching (ACQ) phenomenon commonly observed in traditional organic molecules and materials. AIE luminogens show a weak PL emission in a solution state but an extremely strong PL emission (some even reach unity quantum yield (QY)) in the aggregated state (solid state).[36, 38, 39, 41] Hence, they can be readily used in the solid state with all the native emission properties existing. Such properties of AIE molecules have led to the birth of efficient organic molecules capable of working as molecular machines, sensors, photodetectors, LEDs, solar concentrators and many others.[36, 41, 42] Furthermore, due to their stabilities,[43-45] this class of organic materials could be readily used with many other inorganic materials to create multifaceted O-I heterostructures.

In this work, we develop O-I heterostructures of AIE-active molecular rotors based on tetraphenylethylene (TPE) core dispersed and restricted in poly(methyl methacrylate) (termed AIEgens) (for chemical synthesis, see ***Supplementary Note 1*** and **Figure S1**) and micromechanical exfoliated monolayer TMDs (WS_2, $MoSe_2$ and WSe_2). We observe a very high PL enhancement in all the tested monolayers of WS_2, $MoSe_2$ and WSe_2 when introduced on top of the molecular rotors. The enhancement ratio, defined as $\boldsymbol{\beta} = \left[\frac{I_{hs} - I_{ml}}{I_{ml}}\right]$ where $\boldsymbol{I_{hs}}$ and $\boldsymbol{I_{ml}}$ are integrated PL intensities from the heterostructures (after subtracting the AIEgen's PL background) and TMDs respectively, could reach up to 950%, 500% and 330% for WS_2, $MoSe_2$ and WSe_2, respectively. In terms of photoexcitation pumping efficiency, $\boldsymbol{\beta}$ values normalized to the fractions of the excitation light separately absorbed in the AIEgen and the TMDs), the reported heterostructures show up to ~360, ~140 and ~80 times for WS_2, $MoSe_2$ and WSe_2 as compared to the photoexcitation process in their pristine monolayers, respectively. The pumping efficiency observed is superior compared to the previously reported organic-TMDs type-I heterostructures,[24, 33] and in contrast to the quenching in type-II heterostructures.[22, 26, 33] We attribute the observations to the defect engineering by the functionalized organic layer and the charge transfer in the created type-I band alignment heterostructures.

RESULTS AND DISCUSSION

First, we demonstrate a significant PL enhancement from WS_2 in AIEgen-WS_2 heterostructures. For a systematic comparison, part of the exfoliated monolayer was transferred on the AIEgen area, whereas the remaining part was on the substrate (**Figure 1A**). Two different lasers with excitation wavelengths of 405 nm (3.06 eV) and 532 nm (2.33 eV) (**Figure S2**) were employed to study the photoexcitation process in the O-I heterostructures. The 532-nm laser can excite the inorganic

layer (WS_2) but not the AIEgen film (due to its wide optical band gap of 2.61 eV as shown in **Figure 1B**), whereas the 405-nm laser can excite both. The absorption spectrum of the AIEgen film is given in **Figure S3A**. **Figure 1C and 1D** show PL enhancements of WS_2 in the O-I heterostructure compared to that of pristine WS_2 under the 532- and 405-nm excitation wavelengths (obtained by averaging PL spectra from a PL map), respectively. It can be observed that the 405-nm excitation gives a much higher improvement in the WS_2 PL intensity compared to the 532-nm excitation, both at the same laser power of ~13 Wcm^{-2}. This is also depicted in the PL integrated intensity maps in **Figure 1F** (an optical microscope image of the sample is shown in **Figure 1E**). Quantitatively, when the AIEgen's PL component is subtracted from the heterostructure's total PL spectrum in **Figure 1C** to obtain the actual pumping with the 405-nm excitation (see **Figure S3B**), approximately one order of magnitude increase in PL emission is realized. Meanwhile, only approximately 2-fold increase is observed with the 532-nm excitation.

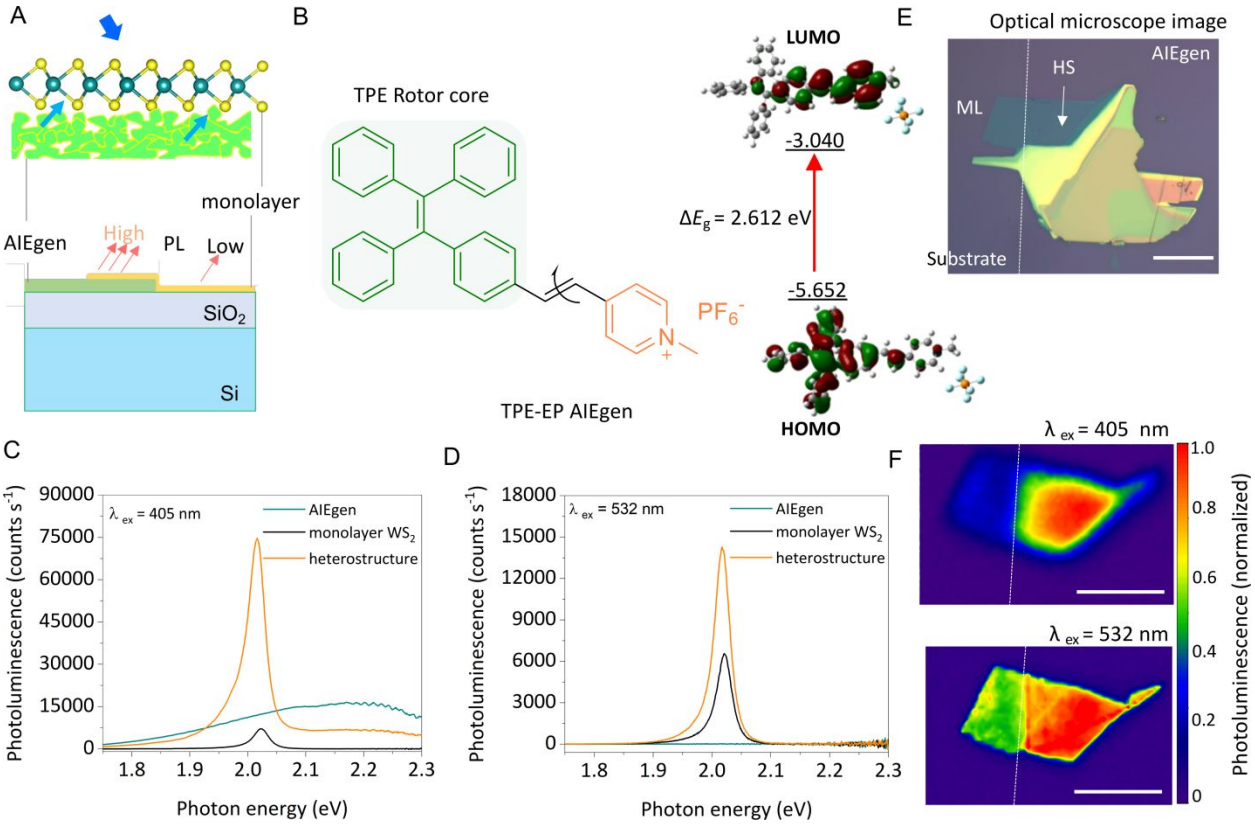

Figure 1. Photoluminescence enhancement in the AIEgen–monolayer WS_2 O-I heterostructure. (A) Schematic showing the arrangement and PL emission from the WS_2 on the AIEgen and on the SiO_2/Si substrate. (B) Chemical structure and simulated spatial plots (see ***Supplementary Note 3***) of TPE-EP AIEgen employed in this work. The calculation of HOMO and LUMO levels is obtained from B3LYP/6-31G* with reference to the vacuum level. The AIEgen has a simulated optical band gap of 2.61 eV, which can potentially form type-I band alignment with WS_2. (C) PL spectra of AIEgen, WS_2 on SiO_2/Si substrate and WS_2 on AIEgen (heterostructure) with the 405-nm excitation and (D) 532-nm excitation. With the 405-nm laser, a wide PL peak of the AIEgen ~2.22 eV can be observed, and its intensity decreases in the heterostructure. With the 532-nm laser, no PL peak is observed from the AIEgen, indicating no excitation process in the AIEgen. (E) Optical microscope image and (F) corresponding normalized PL intensity maps of WS_2 on the SiO_2/Si substrate and on the AIEgen (*i.e.* heterostructure) (in all

images, the scale bar is 25 μm). Part of the monolayer rests on the AIEgen and the remaining part rests on the SiO_2/Si substrate. The intensity value at each pixel was obtained by integrating the PL signal across the spectral window of 1.8–2.2 eV. For both lasers, the power was ~13 Wcm^{-2}. To measure the enhancement at the 405-nm excitation, the AIEgen's background PL spectrum was subtracted from the heterostructure's total PL spectrum.

With the 532-nm excitation, there are few photo-induced carriers inside the AIEgen, as evidenced by the absence of the PL emission from the film (**Figure 1D**). Therefore, we attribute the PL enhancement to defect engineering,[23] surface cleaning (which involves removals of any absorbed water, oxygen, hydroxyl groups and other impurities from the O-I interface due to the protonating nature of a pyridinium salt unit on the rotors),[21] and effects of the dielectric environment[32] under the presence of the organic layer (see ***Supplementary Note 2***). Meanwhile, the much higher enhancement with the 405-nm laser, in addition to the named factors, is mainly due to the AIEgen inducing a type-I band alignment (as later confirmed by PL excitation (PLE) experiments) and hence transferring its photo-generated carriers to the top monolayer WS_2, as illustrated in **Figure 2A**. This improves the PL emission from the top WS_2 with an observed quenching in the AIEgen PL peak of the O-I heterostructure.

Factors affecting the PL enhancement and photoexcitation process are now investigated. The PL intensity of the AIEgen was found to vary with the excitation wavelength**,** excitation power, and AIEgen thickness **(Figure S8)**. Room temperature PLE measurements were used to track the PL enhancement of WS_2 in the heterostructure compared to that on SiO_2/Si substrate, and also to confirm the type-I band alignment in the created O-I hybrid heterostructure. Both the

heterostructure and monolayer WS_2's absorbance and PLE measurements are shown in **Figure 2B**. It can be observed that in both the heterostructure and monolayer, their PL intensity increases when the excitation energy is in resonance with the absorption peak of the B exciton. This behavior is attributed to the spontaneous separation of electrons and holes in the k-space because of the band nesting.[46, 47] Meanwhile, a slight increase in absorption at the A exciton peak with a shift towards higher energies is also observed, possibly due to the underlying AIEgen layer.

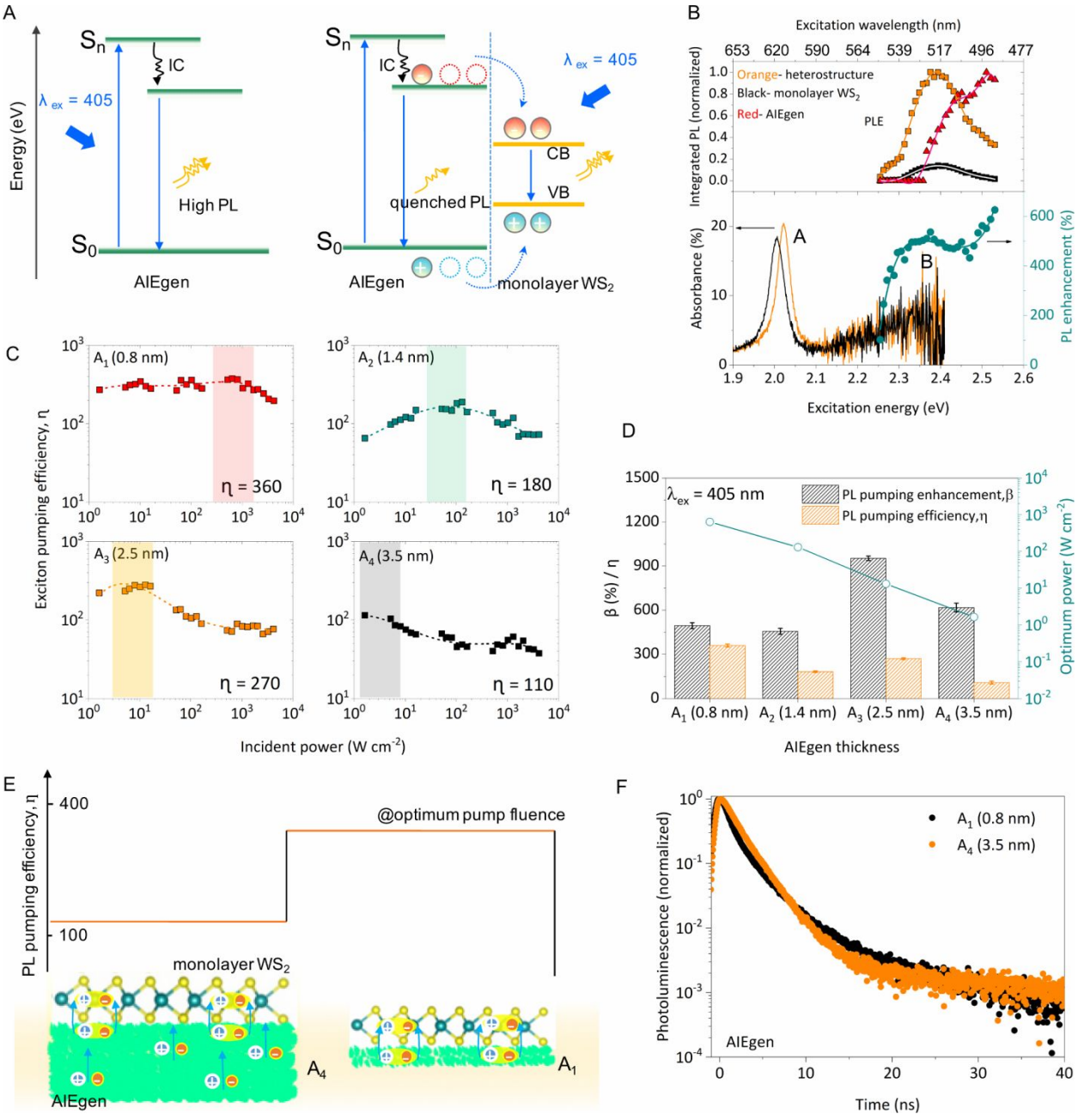

Figure 2. Excitonic PL enhancement dynamics in AIEgen-WS_2 O-I heterostructures. (A) The proposed band illustration of the photoexcitation process in the AIEgen before (left) and after (right) the monolayer incorporation. S_n is the electronic state of resonance when the flurophores are excited with the 405-nm source. S_0 is the electronic ground state. In the neat AIEgen, a strong PL intensity is observed due to a total emission (without any interruption) after an internal

conversion (IC) of molecules' relaxation prior to falling back to the vibration states in S_0. However, the quenching of the AIEgen's PL in the O-I heterostructure is due to only part of the carrier population falling back to S_0 and the remaining part crossing to the inorganic side of the monolayer. This consequently improves the PL emission in the monolayer. (B) Absorbance (full line), PLE (squares and triangles), and PL enhancement (dots) in the O-I hybrid heterostructure (orange) in comparison to the pristine monolayer WS_2 on a SiO_2/Si substrate (black). (C) Power-dependent exciton pumping efficiency η in heterostructures with different AIEgen thicknesses, excited by the 405–nm laser. (D) Comparisons between the maximum PL enhancement β and pumping efficiency η from the heterostructures, together with the corresponding optimum excitation power for each film thickness. (E) The schematic visualizing the charge transfer process in the AIEgen of 0.8-nm and 3.5-nm thicknesses at optimum pump fluencies. (F) Time-resolved PL decay curves used to determine charge lifetimes of AIEgen films. The lifetime was found to be almost the same (~2.1 ns) for all film thicknesses.

The PL enhancement ratio (β) increases with increasing excitation energies and shows a local maximum at the B exciton peak (**Figure 2B**, bottom panel). There are several notable features in this PL enhancement curve. First, there is a sharp reduction in the enhancement at the excitation wavelengths beyond ~528 nm (below ~2.35 eV). PLE measurements of the AIEgen (**Figure S8A)** confirm that the excitation energy below this threshold (~528 nm or 2.35 eV) cannot excite the AIEgen. Consequently, photo-induced carriers are not created in the organic side, causing the sharp decrease in the PL pumping in the O-I heterostructure at the 528-nm excitation wavelength and beyond. The abrupt switching between the strong and weak enhancements at ~528-nm excitation confirms the type-I band alignment and interfacial charge transfer process in the O-I

heterostructure. Second, the local maximum of the enhancement curve (~523 nm or 2.37 eV) before the sharp decrease coincides well with the absorption B exciton peak of the monolayer WS_2. This means that the absorption features in the O-I heterostructure are similar to those in WS_2, with exciton resonance absorption peak B existing due to the band nesting.[46, 47] Therefore, it is logical to expect a PL enhancement when the carriers are excited in this band nesting region. This explains why despite the falling trend in the PL emission in the AIEgen with decreasing excitation energies (**Figure S8A**), we do not necessarily see the same trend in the heterostructure, but the local PL enhancement (**Figure 2B**, bottom panel) at the WS_2's B exciton peak.

Next, we compare PL pumping efficiencies (η) of different heterostructures of WS_2 fabricated with various thicknesses of the AIEgen under different pump fluencies (between 10^0 and 10^4 Wcm^{-2}), as shown in **Figure 2C**. Their atomic force microscope (AFM) images and height analysis are shown in **Figure S9**. Here, we define the PL pumping efficiency (η) to be the enhancement ratio (β) normalized to the fractions of the excitation light separately absorbed in the AIEgen and monolayer. This parameter η is calculated according to **Equation 1** and represents how efficient light is utilized in the materials under study.

$$\text{PL pumping efficiency } (\eta) = \text{PL enhancement } (\beta) \times \left[\frac{A_{ml}}{A_{AIEgen}}\right] = \left[\frac{I_{hs} - I_{ml}}{I_{ml}}\right] \times \left[\frac{A_{ml}}{A_{AIEgen}}\right] \quad (1).$$

A_{ml} and A_{AIEgen} represent the measured absorption values from the monolayer and AIEgen at 405 nm, respectively (see ***Supplementary Note 4*** and **Table S1**). The PL enhancement (β) chart at various pump fluencies for four WS_2-based heterostructures on 0.8, 1.4, 2.5, and 3.5-nm AIEgen

thicknesses is provided in **Figure S10**. The maximum PL enhancement β in the AIEgen-WS_2 heterostructure has the following trend (thickness (β)): 2.5 nm (950%) > 3.5 nm (620%) > 0.8 nm (500%) > 1.4 nm (460%). These maximum values happen at different optimum pump fluencies (**Figure S10)**. Several samples (N > 4) were tested and the results were repeatable. It is also worth noting that the organic AIEgen layer was stable in air over the tested period of 11 weeks (**Figure S11**), indicating its superiority over the previously reported organic interfaces.[24] In fact, the excellent air stability has made the AIE to be very popular and versatile for a wide range of optoelectronic, biological and physiochemical applications.[43-45] The exciton pumping efficiency (η) values are then calculated and plotted in **Figure 2C** for various pump fluencies. However, the η trend is different from the β trend in the tested samples. This is due to the increased absorption at the 405-nm excitation wavelength in thicker AIEgen organic layers (**Table S1**). The maximum pumping efficiency η (in times) has the following trend (thickness (η)): 0.8 nm (360) > 2.5 nm (270)> 1.4 nm (180) > 3.5 nm (110). A comparison chart between the maximum PL pumping efficiency and enhancement in different heterostructures on the four AIEgen thicknesses, together with the optimum power, is provided in **Figure 2D (**for their corresponding PL spectra, see **Figure S13 (**with the corresponding PL QY). We observe that the optimum laser power required for the maximum β and η decreases with increasing AIEgen thicknesses. Thicker AIEgen layers have more restricted rotors and thus need less power to create enough carriers at the O-I interface responsible for the interfacial charge transfer process. The opposite is true for thinner AIEgen layers. Also, η in the 2.5-nm sample is similar to that of the 1.4-nm sample, while the β of the former is over two times more than that of the latter. This is because η also accounts for the excitation absorption in the AIEgen. Overall, the observed pumping efficiency η in the our

AIEgen-based heterostructures is much higher than the previously reported values on 2D TMDs-based O-I heterostructures.[23-29, 31]

Moreover, we continue hypothesizing the charge transfer mechanism (**Figure 2E**) in the different AIEgen thicknesses based on the PL, excitation power dependence, and lifetime measurements. In general, there can be three possible mechanisms[24, 48-50] across the O-I interface. First, the excited charges in the organic layer are highly mobile. They can move laterally within this layer for a long distance before returning to the ground state, and hence hardly cross the O-I interface. Second, the excited organic charges are slightly mobile. They can move a short distance laterally and then are still able to cross the O-I interface. Third, these charges are immobile in the organic layer hence can efficiently cross the O-I interface. In our work, the decay lifetime curves from the AIEgen films with different thicknesses are identical, meaning that the charge diffusion length in these films is the same (**Figure 2F**). Therefore, the charge transfer mechanism should be the same across all the O-I heterostrutures built on different AIEgen thicknesses. Morever, the AIEgen has a highly twisted structure which restricts the intermolecular π-π interactions in the aggregate state.[38] Most photo-excited carriers in the AIEgen rotors of the organic layer tend to be immobile in the horizontal plane within the AIEgen. In this sense, the third mechanism likely dominates in our O-I heterostructures. Therefore, the PL pumping efficiency is high for all AIEgen thicknesses. However, in thicker AIEgen films (e.g., ~3.5 nm), although more photo-excited carriers are created in the AIEgen layer as evidenced by the PL results (**Figure S8C**), the charges need to move a longer vertical distance (illustrated in **Figure 2E**), resulting in a lower percentage crossing the O-I interface.[48]

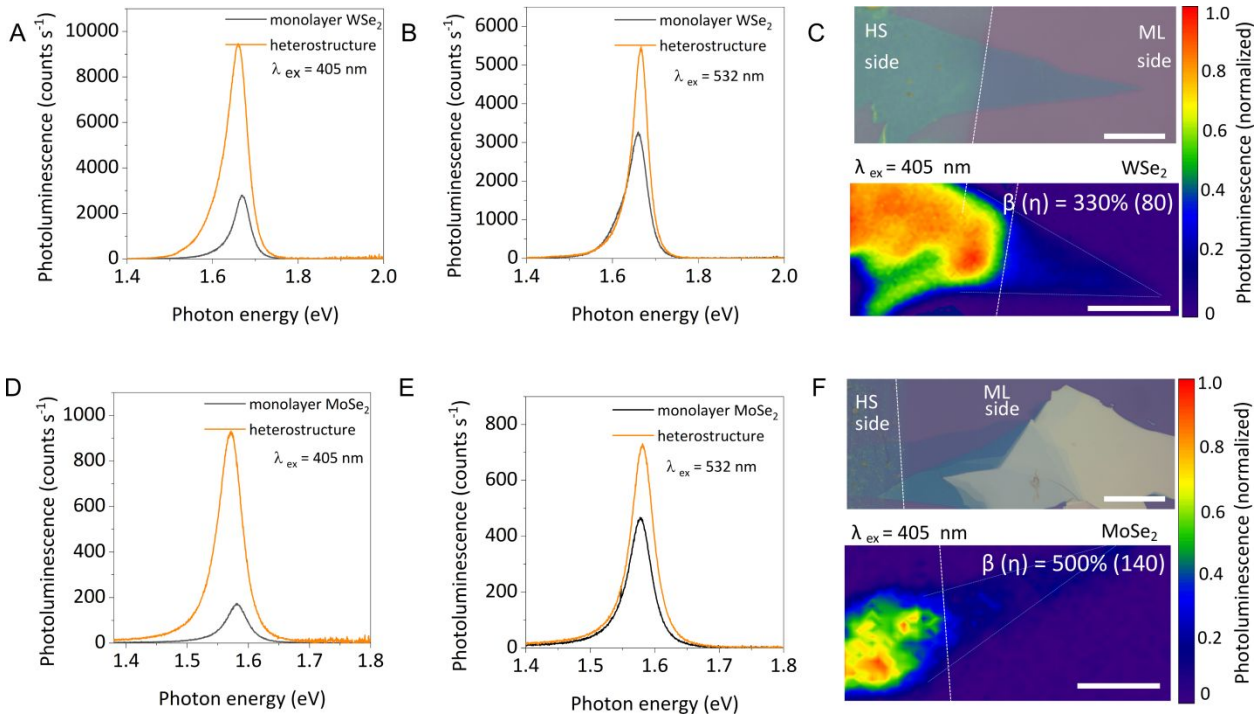

Figure 3. Excitonic PL enhancement in AIEgen-WSe_2 and AIEgen-$MoSe_2$ O-I heterostructures. (A) PL spectra of WSe_2 and AIEgen-WSe_2 O-I heterostructure with 405-nm and (B) 532-nm excitation, and (C) their corresponding optical microscope image and PL integrated intensity map (scale bar: 25 um). (D-F) Similar data for $MoSe_2$. The boundaries between the monolayers (ML) and heterostructures (HS) are shown as the vertical dash lines in these images. The regions created by the three dashed lines in C and F represent the monolayers in the PL maps. Note that for the PL spectra presented in A and D, the AIEgen's background PL signal has been subtracted for clarity. The original PL spectra before the background subtraction are shown in **Figure S14**.

Now, we demonstrate that the AIEgen-assisted exciton pumping effects are universal for other monolayer TMDs including WSe_2 and $MoSe_2$ (**Figure 3**). Similar to WS_2, WSe_2 and $MoSe_2$-based O-I heterostructures show very strong PL enhancements with β values of ~330% and ~500% and corresponding η values (β values normalized to the fractions of the excitation light separately absorbed in the AIEgen and monolayer) of ~80 and 140 times, respectively. Their corresponding PL spectra are shown in **Figure 3A-B** and **3D-E** (after subtracting the AIEgen's background PL signal) and PL integrated intensity maps in **Figure 3C** and **3F** for WSe_2 and $MoSe_2$-based heterostructures, respectively. Same as in the AIEgen-WS_2 samples, with the 405-nm excitation (**Figure 3A** and **3D**), the enhancement in the O-I heterostructures is stronger compared to the 532-nm excitation (**Figure 3B** and **3E**). This is again due to the AIEgen-assisted pumping effect in the type-I band alignment O-I heterostructures. With the 405-nm excitation, there are photogenerated carriers in the AIEgen layer, and they can efficiently transfer into the TMD inorganic layer, leading to an increased carrier population and hence the enhanced excitonic PL emission. Meanwhile, the less significant enhancement with the 532-nm excitation is mainly from the defect engineering,[23] surface cleaning,[21] and effects of the dielectric environment[32] due to the presence of the organic layer. Note that in this study, we present only one exemplary type of AIE families. Various AIE types can be tuned to have different HOMO and LUMO levels, yielding different wavelength-dependent PL enhancements in their respective heterostructures.

Since our preliminary results show a very strong PL enhancement, we continue investigating effects of the PL pumping on some important photovoltaic properties of the AIEgen-WS_2-based O-I heterostructure including quasi-Fermi level splitting values under illumination ($\Delta\mu$) and minority carrier lifetimes. The former parameter $\Delta\mu$ can be extracted from the relationship

between the emission $dr_{em}(\hbar\omega)$ and absorption $A(\hbar\omega)$ spectra, according to the generalized Planck law:[51-55]

$$dr_{em}(\hbar\omega) = A(\hbar\omega) \times \frac{(\hbar\omega)^2}{4\pi^2\hbar^3c^2} \times \left[\exp\left(\frac{\hbar\omega - \Delta\mu}{kT}\right) - 1\right]^{-1} \quad (2)$$

where $\hbar$, k, c, and T are the reduced Planck constant, Boltzmann's constant, speed of light, and absolute temperature of the sample, respectively.

The absorption curves of the heterostructure with various AIEgen thicknesses are given in **Figure S12**. The method to extract these absorption curves is described in ***Supplementary Note 4***. There is a slight absorption improvement in the heterostructure compared to the pristine monolayer ascribed to the presence of the inorganic layer beneath the TMD monolayers. From the PL and absorption spectra from each location in the heterostructure (see **Figure 4A** for representative spectra), a $\Delta\mu$ map can be extracted using **Equation 2**. The details on how to extract $\Delta\mu$ are given in ***Supplementary Note 5*** and ***6***, or our previous work.[54] The corresponding integrated PL intensity and absorption maps are given in **Figure S15**. Under real sunlight exposure, the $\Delta\mu$ parameter of a certain material reflects the maximum open-circuit voltage ($V_{oc,max}$) which a solar cell fabricated from that material can possibly achieve, assuming no loss during the cell fabrication process. Under the monochromatic excitation in this work, $\Delta\mu$ is not an exact representative of $V_{oc,max}$ of a solar cell, but it should give some indication for the potential of the material. The $\Delta\mu$ map is given in **Figure 4B**. From the map, an average $\Delta\mu$ value of ~1456 ± 4 meV can possibly be achieved for the formed AIEgens-WS_2-based heterostructure. This value is slightly higher than the value obtained in the pristine monolayer WS_2 (~1400 ± 5 meV) in our previous reported results.[54]

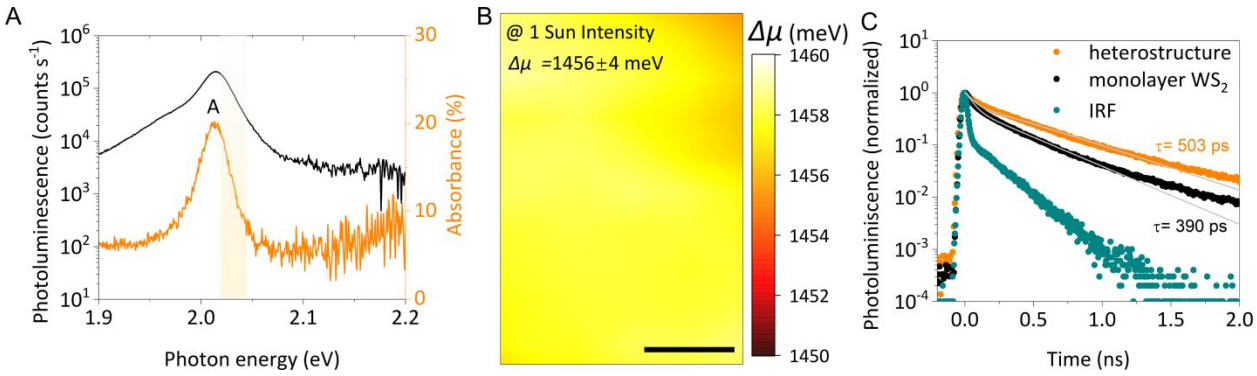

Figure 4. Photovoltaic properties of the AIEgen-WS_2-based O-I heterostructure. (A) Representative PL and absorption spectra from the heterostructure at room temperature. Using the generalized Planck law, the quasi-Fermi level splitting $\Delta\mu$ under excitation can be extracted. "A" denotes the A-excitonic peak. The excitation wavelength is 405 nm and the excitation intensity is 16 Suns. In this work, 1 Sun is defined as 0.1W/cm^2 equivalent intensity. (B) The resultant $\Delta\mu$ map of a AIEgen-WS_2 heterostructure-based solar cell. Note that the obtained values of $\Delta\mu$ were all corrected for a 1-Sun intensity, which is relevant to evaluating performances of photovoltaic devices, using the formula $\Delta\mu_{@\ 1\text{sun}} = \Delta\mu_{@\ 16\ \text{suns}} - (1/kT)\times ln(16)$. The scale bar is 2.5 um. (C) Lifetime measurements of the heterostructure and pristine WS_2 regions, excited with a 522-nm femto-second laser.

Finally, time-resolved PL measurements on the pristine WS_2 and heterostructure, both prepared from the same monolayer on the same substrate (part of the monolayer is directly placed on the SiO_2/Si substrate, the remaining is on the AIEgen film), show a significant carrier lifetime improvement in the latter. The pristine monolayer WS_2 shows a shorter decay lifetime (390 ps), after accounting for the instrument response function (IRF), compared to the heterostructure (503

ps) (**Figure 4C**). The increased lifetime in the heterostructure can be ascribed to the defect treatment and surface cleaning of the monolayer under the presence of the organic film. Similar results after chemical treatments have been previously reported for monolayer semiconductors.[21, 24]

CONCLUSION

In summary, we have demonstrated significant exciton luminescence pumping in atomically thin TMDs by fabricating efficient O-I heterostructures based on AIE molecular rotors. The reported results shed light on the possibility of utilizing the stable, high emission AIEgens in an aggregated state. This approach improves the low excitonic luminescence efficiency of the inorganic two-dimensional monolayer semiconductors due to their defects and strong quasi-multiparticle formations which promote nonradiative recombination. The hybrid O-I heterostructures improve not only the luminescence in the monolayer semiconductors but also their photovoltaic properties, including the quasi-Fermi level splitting, absorption and minority carrier lifetime. With the demonstrated excellent stability, rich functionality, and diversity of AIE families, these O-I heterostructures could be employed in a wide range of optoelectronic applications such as solar cells, photodetectors, LEDs, optical sensors and many others.

EXPERIMENTAL SECTION

TMD monolayer preparation. From the bulk crystals of specific TMDs (HQ Graphene®), monolayers of WS_2, $MoSe_2$ and WSe_2 were obtained using a micro-mechanical exfoliation technique. The technique employed a scotch tape to exfoliate multi-layered crystals placed on a clean gel substrate (Gel-Pak®) into very thin materials with few to monolayers. Monolayers of TMDs were first identified using an optical contrast technique and later confirmed by Raman, PL,

and AFM measurements. After that, the obtained monolayer TMDs were transferred from the gel film into a target cleaned substrate (either quartz or Si/SiO_2) for required measurements.

AIEgen layer preparation. A 2 wt% AIEgen solution prepared according to ***Supplementary Note 1*** in chloroform was employed. Using a spin-coater (LOR3A) with varying speeds (7500-8500 rpm) and varying times (10-30 s), four film thicknesses were obtained. To create two interfaces with and without the AIEgen film on the same sample, all substrates were first cut in sizes of 1 cm × 1 cm. The AIEgen solution was dropped at the edge of a high-speed moving substrate, forming a clear circular pattern in the substrate center without the AIEgen and leaving the edges with the AIEgen. Then monolayer TMDs were transferred onto boundaries between the AIEgen film and bare substrate to form both pristine monolayers and AIEgen-monolayer heterostructures. Before the monolayers were transferred onto the AIEgen films, the films were left in the air for at least 5 hrs for the chloroform to completely evaporate, ensuring dry surfaces.

Optical measurements. Micro-photoluminescence (micro-PL) spectroscopy was performed using a Horiba LabRAM system equipped with a confocal microscope, a charge-coupled device (CCD) Si detector (detection range between 400 – 1000 nm), and a 40× reflective objective lens (numerical aperture = 0.5). The excitation sources were continuous-wave 532-nm and 405-nm diode-pumped solid-state (DPSS) lasers. For PL excitation (PLE) measurements, a supercontinuum excitation light source (NKT SuperK ®Extreme EXR-20) with a tuneable wavelength range between 490 and 2000 nm was employed. In this work, excitation wavelengths between 490 and 550 nm were used, and the on-sample power was kept constant for all excitation wavelengths. The wavelength selection was achieved using a SuperK VARIA attachment allowing the tuning of both the center wavelength and bandwidth of the filtered light. The spectral response of the entire system was determined with a calibrated tungsten-halogen light source. The PL

spectra were all corrected for the spectral response of the system. All measurements in this work were performed at room temperature. Time-resolved PL (TRPL) measurements were conducted using a custom built system consisting of a pulsed laser (522 nm, 300 fs pulse width, and 20.8 MHz repetition rate), a high numerical aperture (NA = 0.7) objective (Nikon S Plan, 60×), a grating spectrometer, a Si single-photon avalanche diode, and a time-correlated single-photon counting (TCSPC, PicoHarp 300) system with a time resolution of 20 ps. The reflectance spectra of the monolayer TMDs, heterostructures, and substrates were measured using the same μ-PL system with a broadband illumination from the supercontinuum NKT SuperK laser. The measured differential reflectance spectra from the substrates and samples were then used to obtain the absorbance spectra (see ***Supplementary Note 4***).

Other techniques. The atomic force microscopy (AFM) images were collected by a Bruker Dimension Icon scanning probe microscope system. A SCANASYST-AIR tip (spring constant 0.2-0.8 N m^{-1}) operates in tapping mode at a resonant frequency of 45-95 kHz. A scan an area of 10×10 μm^2 was acquired which was set to have 1,024 points on the fast axis and 256 lines on the slow axis with a scan rate of 0.5 Hz. The scan locations were guided by optical images.

ASSOCIATED CONTENT

The Supporting Information is available free of charge at https://pubs.acs.org/doi/10.1021/acsnano.xxxxxxx

The file is 23 pages and it includes; Supplementary Notes 1 to 6 providing more details of experiments, characterizations and material perfomance, including; (1) Chemical synthesis and preparation of AIEgens; (2) Effects of substrates, laser wavelengths and AIEgen films on PL peak positions of the samples; (3) Simulation of spatial plots of AIEgen; (4) Absorption measurements of AIEgen films, heterostructures, and monolayer TMDs; (5) Extraction of $\Delta\mu$ in the heterostructure; (6) Determination of scaling factor (SF). Scheme 1 for the synthetic route of TPE-

EP. Figures S1 to S17, including; (S1) WAXD pattern; S2-S8, S10-S14, S16-S17- various PL, absorption spectra, and analysis of PL/absorption plots and maps; S9- AFM image analysis; S15- $\Delta\mu$ map of the AIEgen-WS_2 heterostructure on a quartz substrate. Table S1- Absorption of the AIEgen films and monolayer TMDs at 405 nm and Table S2- Values of parameters used for establishing the SF. (PDF)

AUTHOR INFORMATION

Corresponding Authors*

Mike Tebyetekerwa (mike.tebyetekerwa@anu.edu.au)

Hieu T. Nguyen (hieu.nguyen@anu.edu.au)

Author Contributions

M.T. and H.T.N. conceived the idea and designed the overall experiments. H.T.N. supervised the project. D.M. and Y.L. consulted the scientific direction and co-supervised the project. M.T. fabricated the TMD samples and performed all the optical-based measurements. Y.C., W.L., and H.L synthesized the AIEgen used in this work and together contributed towards the AIE-related discussion of this article. C.X. and M.M.A. carried out all the AFM measurements. Z.Y., J.Z., B.W., G.P.N., and T.N.T. contributed to the 2D material fabrication and some experimental setups. M.T. and H.T.N. performed the quasi-Fermi splitting simulations. Y.C. simulated spatial plots of the AIEgen. M.T. and H.T.N. analyzed the data and together with Y.C. wrote the manuscript. All authors contributed to the discussion of the results, reviewed the manuscript and have given approval to the final version of the manuscript.

ACKNOWLEDGMENTS

This work is funded by the Australian Renewable Energy Agency (ARENA, RND017) and partially supported by the National Science Foundation of China (51973030). M.T. acknowledges

the research support of the Australian Government Research Training Program (RTP) Scholarship. H.T.N. acknowledges the fellowship support from the Australian Centre for Advanced Photovoltaics (ACAP). We greatly appreciate *Z. Yang, K. Ye, A. A. Wibowo, and R. Premayogi* for their efforts in micromechanical exfoliation of some ML samples used in this work

REFERENCES

1. Wang, Q. H.; Kalantar-Zadeh, K.; Kis, A.; Coleman, J. N.; Strano, M. S., Electronics and Optoelectronics of Two-Dimensional Transition Metal Dichalcogenides. *Nat. Nanotechnol.* **2012,** *7*, 699-712.

2. Wilson, J. A.; Yoffe, A., The Transition Metal Dichalcogenides Discussion and Interpretation of the Observed Optical, Electrical and Structural Properties. *Adv. Phys.* **1969,** *18*, 193-335.

3. Yoffe, A., Layer Compounds. *Annu. Rev. Mater. Sci.* **1973,** *3*, 147-170.

4. Duan, X.; Wang, C.; Pan, A.; Yu, R.; Duan, X., Two-Dimensional Transition Metal Dichalcogenides as Atomically Thin Semiconductors: Opportunities and Challenges. *Chem. Soc. Rev.* **2015,** *44*, 8859-8876.

5. Wang, L.; Huang, L.; Tan, W. C.; Feng, X.; Chen, L.; Huang, X.; Ang, K.-W., 2D Photovoltaic Devices: Progress and Prospects. *Small Methods* **2018,** *2*, 1700294.

6. Mak, K. F.; He, K.; Shan, J.; Heinz, T. F., Control of Valley Polarization in Monolayer MoS_2 by Optical Helicity. *Nat. Nanotechnol.* **2012,** *7*, 494.

7. Cao, T.; Wang, G.; Han, W.; Ye, H.; Zhu, C.; Shi, J.; Niu, Q.; Tan, P.; Wang, E.; Liu, B., Valley-Selective Circular Dichroism of Monolayer Molybdenum Disulphide. *Nat. Commun.* **2012,** *3*, 887.

8. Choi, W.; Choudhary, N.; Han, G. H.; Park, J.; Akinwande, D.; Lee, Y. H., Recent

Development of Two-Dimensional Transition Metal Dichalcogenides and Their Applications. *Mater. Today* **2017,** *20*, 116-130.

9. Bhimanapati, G. R.; Lin, Z.; Meunier, V.; Jung, Y.; Cha, J.; Das, S.; Xiao, D.; Son, Y.; Strano, M. S.; Cooper, V. R.; Liang, L.; Louie, S. G.; Ringe, E.; Zhou, W.; Kim, S. S.; Naik, R. R.; Sumpter, B. G.; Terrones, H.; Xia, F.; Wang, Y.*, et al.*, Recent Advances in Two-Dimensional Materials Beyond Graphene. *ACS Nano* **2015,** *9*, 11509-39.

10. Wang, Q. H.; Kalantar-Zadeh, K.; Kis, A.; Coleman, J. N.; Strano, M. S., Electronics and Optoelectronics of Two-Dimensional Transition Metal Dichalcogenides. *Nat. Nanotechnol.* **2012,** *7*, 699.

11. Xia, F.; Wang, H.; Xiao, D.; Dubey, M.; Ramasubramaniam, A., Two-Dimensional Material Nanophotonics. *Nat. Photonics* **2014,** *8*, 899.

12. Britnell, L.; Ribeiro, R. M.; Eckmann, A.; Jalil, R.; Belle, B. D.; Mishchenko, A.; Kim, Y. J.; Gorbachev, R. V.; Georgiou, T.; Morozov, S. V.; Grigorenko, A. N.; Geim, A. K.; Casiraghi, C.; Neto, A. H. C.; Novoselov, K. S., Strong Light-Matter Interactions in Heterostructures of Atomically Thin Films. *Science* **2013,** *340*, 1311.

13. Alexeev, E. M.; Ruiz-Tijerina, D. A.; Danovich, M.; Hamer, M. J.; Terry, D. J.; Nayak, P. K.; Ahn, S.; Pak, S.; Lee, J.; Sohn, J. I.; Molas, M. R.; Koperski, M.; Watanabe, K.; Taniguchi, T.; Novoselov, K. S.; Gorbachev, R. V.; Shin, H. S.; Fal'ko, V. I.; Tartakovskii, A. I., Resonantly Hybridized Excitons in Moiré Superlattices in van der Waals Heterostructures. *Nature* **2019,** *567*, 81-86.

14. Merkl, P.; Mooshammer, F.; Steinleitner, P.; Girnghuber, A.; Lin, K. Q.; Nagler, P.; Holler, J.; Schüller, C.; Lupton, J. M.; Korn, T.; Ovesen, S.; Brem, S.; Malic, E.; Huber, R., Ultrafast Transition between Exciton Phases in van der Waals Heterostructures. *Nat. Mater.* **2019,** *18*, 691-

696.

15. Lee, C.-H.; Lee, G.-H.; Van Der Zande, A. M.; Chen, W.; Li, Y.; Han, M.; Cui, X.; Arefe, G.; Nuckolls, C.; Heinz, T. F., Atomically Thin *p-n* Junctions with van der Waals Heterointerfaces. *Nat. Nanotechnol.* **2014,** *9*, 676.

16. Lin, Y.-C.; Ghosh, R. K.; Addou, R.; Lu, N.; Eichfeld, S. M.; Zhu, H.; Li, M.-Y.; Peng, X.; Kim, M. J.; Li, L.-J., Atomically Thin Resonant Tunnel Diodes Built from Synthetic van der Waals Heterostructures. *Nat. Commun.* **2015,** *6*, 7311.

17. Geim, A. K.; Grigorieva, I. V., van der Waals Heterostructures. *Nature* **2013,** *499*, 419.

18. Novoselov, K.; Mishchenko, A.; Carvalho, A.; Neto, A. C., 2D Materials and van der Waals Heterostructures. *Science* **2016,** *353*, aac9439.

19. Wang, H.; Zhang, C.; Rana, F., Ultrafast Dynamics of Defect-Assisted Electron–Hole Recombination in Monolayer MoS_2. *Nano Lett.* **2014,** *15*, 339-345.

20. Lien, D.-H.; Uddin, S. Z.; Yeh, M.; Amani, M.; Kim, H.; Ager, J. W.; Yablonovitch, E.; Javey, A., Electrical Suppression of All Nonradiative Recombination Pathways in Monolayer Semiconductors. *Science* **2019,** *364*, 468-471.

21. Amani, M.; Lien, D.-H.; Kiriya, D.; Xiao, J.; Azcatl, A.; Noh, J.; Madhvapathy, S. R.; Addou, R.; Santosh, K.; Dubey, M., Near-Unity Photoluminescence Quantum Yield in MoS_2. *Science* **2015,** *350*, 1065-1068.

22. Jariwala, D.; Marks, T. J.; Hersam, M. C., Mixed-Dimensional van der Waals Heterostructures. *Nat. Mater.* **2016,** *16*, 170.

23. Cho, K.; Pak, J.; Chung, S.; Lee, T., Recent Advances in Interface Engineering of Transition-Metal Dichalcogenides with Organic Molecules and Polymers. *ACS Nano* **2019,** *13*, 9713-9734.

24. Zhang, L.; Sharma, A.; Zhu, Y.; Zhang, Y.; Wang, B.; Dong, M.; Nguyen, H. T.; Wang, Z.; Wen, B.; Cao, Y., Efficient and Layer-Dependent Exciton Pumping across Atomically Thin Organic–Inorganic Type-I Heterostructures. *Adv. Mater.* **2018,** *30*, 1803986.

25. Jariwala, D.; Howell, S. L.; Chen, K.-S.; Kang, J.; Sangwan, V. K.; Filippone, S. A.; Turrisi, R.; Marks, T. J.; Lauhon, L. J.; Hersam, M. C., Hybrid, Gate-Tunable, van der Waals *p-n* Heterojunctions from Pentacene and MoS_2. *Nano Lett.* **2015,** *16*, 497-503.

26. Bettis Homan, S.; Sangwan, V. K.; Balla, I.; Bergeron, H.; Weiss, E. A.; Hersam, M. C., Ultrafast Exciton Dissociation and Long-Lived Charge Separation in a Photovoltaic Pentacene–MoS_2 van der Waals Heterojunction. *Nano Lett.* **2016,** *17*, 164-169.

27. Zhu, T.; Yuan, L.; Zhao, Y.; Zhou, M.; Wan, Y.; Mei, J.; Huang, L., Highly Mobile Charge-Transfer Excitons in Two-Dimensional WS_2/Tetracene Heterostructures. *Sci. Adv.* **2018,** *4*, eaao3104.

28. Liu, X.; Gu, J.; Ding, K.; Fan, D.; Hu, X.; Tseng, Y.-W.; Lee, Y.-H.; Menon, V.; Forrest, S. R., Photoresponse of an Organic Semiconductor/Two-Dimensional Transition Metal Dichalcogenide Heterojunction. *Nano Lett.* **2017,** *17*, 3176-3181.

29. Liu, F.; Chow, W. L.; He, X.; Hu, P.; Zheng, S.; Wang, X.; Zhou, J.; Fu, Q.; Fu, W.; Yu, P., van der Waals *p-n* Junction Based on an Organic–Inorganic Heterostructure. *Adv. Funct. Mater.* **2015,** *25*, 5865-5871.

30. Park, S.; Schultz, T.; Xu, X. M.; Wegner, B.; Aljarb, A.; Han, A.; Li, L. J.; Tung, V. C.; Amsalem, P.; Koch, N., Demonstration of the Key Substrate-Dependent Charge Transfer Mechanisms between Monolayer MoS_2 and Molecular Dopants. *Commun. Phys.* **2019,** *2*, 109.

31. Bertolazzi, S.; Gobbi, M.; Zhao, Y.; Backes, C.; Samorì, P., Molecular Chemistry Approaches for Tuning the Properties of Two-Dimensional Transition Metal Dichalcogenides.

Chem. Soc. Rev. **2018,** *47*, 6845-6888.

32. Schlesinger, R.; Bianchi, F.; Blumstengel, S.; Christodoulou, C.; Ovsyannikov, R.; Kobin, B.; Moudgil, K.; Barlow, S.; Hecht, S.; Marder, S., Efficient Light Emission from Inorganic and Organic Semiconductor Hybrid Structures by Energy-Level Tuning. *Nat. Commun.* **2015,** *6*, 6754.

33. Huang, Y. L.; Zheng, Y. J.; Song, Z.; Chi, D.; Wee, A. T. S.; Quek, S. Y., The Organic-2D Transition Metal Dichalcogenide Heterointerface. *Chem. Soc. Rev.* **2018,** *47*, 3241-3264.

34. Zhao, Z.; Zheng, X.; Du, L.; Xiong, Y.; He, W.; Gao, X.; Li, C.; Liu, Y.; Xu, B.; Zhang, J.; Song, F.; Yu, Y.; Zhao, X.; Cai, Y.; He, X.; Kwok, R. T. K.; Lam, J. W. Y.; Huang, X.; Lee Phillips, D.; Wang, H.*, et al.*, Non-Aromatic Annulene-Based Aggregation-Induced Emission System *via* Aromaticity Reversal Process. *Nat. Commun.* **2019,** *10*, 2952.

35. Qi, J.; Li, J.; Liu, R. H.; Li, Q.; Zhang, H. K.; Lam, J. W. Y.; Kwok, R. T. K.; Liu, D. B.; Ding, D.; Tang, B. Z., Boosting Fluorescence-Photoacoustic-Raman Properties in One Fluorophore for Precise Cancer Surgery. *Chem* **2019,** *5*, 2657-2677.

36. Hong, Y.; Lam, J. W.; Tang, B. Z., Aggregation-Induced Emission. *Chem. Soc. Rev.* **2011,** *40*, 5361-5388.

37. Khorloo, M.; Cheng, Y.; Zhang, H.; Chen, M.; Sung, H. H. Y.; Williams, I. D.; Lam, J. W. Y.; Tang, B. Z., Polymorph Selectivity of an Aie Luminogen under Nano-Confinement to Visualize Polymer Microstructures. *Chem. Sci.* **2020,** *11*, 997-1005.

38. Mei, J.; Leung, N. L. C.; Kwok, R. T. K.; Lam, J. W. Y.; Tang, B. Z., Aggregation-Induced Emission: Together We Shine, United We Soar! *Chem. Rev.* **2015,** *115*, 11718-11940.

39. Qian, J.; Tang, B. Z., AIE Luminogens for Bioimaging and Theranostics: From Organelles to Animals. *Chem* **2017,** *3*, 56-91.

40. Cheng, Y. H.; Liu, S. J.; Song, F. Y.; Khorloo, M.; Zhang, H. K.; Kwok, R. T. K.; Lam, J.

W. Y.; He, Z. K.; Tang, B. Z., Facile Emission Color Tuning and Circularly Polarized Light Generation of Single Luminogen in Engineering Robust Forms. *Mater. Horiz.* **2019,** *6*, 405-411.

41. Hong, Y.; Lam, J. W.; Tang, B. Z., Aggregation-Induced Emission: Phenomenon, Mechanism and Applications. *Chem. Commun.* **2009**, 4332-4353.

42. Hu, R.; Leung, N. L.; Tang, B. Z., Aie Macromolecules: Syntheses, Structures and Functionalities. *Chem. Soc. Rev.* **2014,** *43*, 4494-562.

43. Zhu, Z.; Qian, J.; Zhao, X.; Qin, W.; Hu, R.; Zhang, H.; Li, D.; Xu, Z.; Tang, B. Z.; He, S., Stable and Size-Tunable Aggregation-Induced Emission Nanoparticles Encapsulated with Nanographene Oxide and Applications in Three-Photon Fluorescence Bioimaging. *ACS Nano* **2016,** *10*, 588-597.

44. Zhao, Z.; Chan, C. Y. K.; Chen, S.; Deng, C.; Lam, J. W. Y.; Jim, C. K. W.; Hong, Y.; Lu, P.; Chang, Z.; Chen, X.; Lu, P.; Kwok, H. S.; Qiu, H.; Tang, B. Z., Using Tetraphenylethene and Carbazole to Create Efficient Luminophores with Aggregation-Induced Emission, High Thermal Stability, and Good Hole-Transporting Property. *J. Mater. Chem.* **2012,** *22*, 4527-4534.

45. Cheng, Y.; Wang, J.; Qiu, Z.; Zheng, X.; Leung, N. L.; Lam, J. W.; Tang, B. Z., Multiscale Humidity Visualization by Environmentally Sensitive Fluorescent Molecular Rotors. *Adv. Mater.* **2017,** *29*, 1703900.

46. Hill, H. M.; Rigosi, A. F.; Roquelet, C.; Chernikov, A.; Berkelbach, T. C.; Reichman, D. R.; Hybertsen, M. S.; Brus, L. E.; Heinz, T. F., Observation of Excitonic Rydberg States in Monolayer MoS_2 and WS_2 by Photoluminescence Excitation Spectroscopy. *Nano Lett.* **2015,** *15*, 2992-2997.

47. Kozawa, D.; Kumar, R.; Carvalho, A.; Kumar Amara, K.; Zhao, W.; Wang, S.; Toh, M.; Ribeiro, R. M.; Castro Neto, A. H.; Matsuda, K.; Eda, G., Photocarrier Relaxation Pathway in

Two-Dimensional Semiconducting Transition Metal Dichalcogenides. *Nat. Commun.* **2014,** *5*, 4543.

48. Zhang, Y.; Qiao, J.; Gao, S.; Hu, F.; He, D.; Wu, B.; Yang, Z.; Xu, B.; Li, Y.; Shi, Y., Probing Carrier Transport and Structure-Property Relationship of Highly Ordered Organic Semiconductors at the Two-Dimensional Limit. *Phys. Rev. Lett.* **2016,** *116*, 016602.

49. Ostroverkhova, O.; Cooke, D.; Shcherbyna, S.; Egerton, R.; Hegmann, F.; Tykwinski, R.; Anthony, J., Bandlike Transport in Pentacene and Functionalized Pentacene Thin Films Revealed by Subpicosecond Transient Photoconductivity Measurements. *Phys. Rev. B* **2005,** *71*, 035204.

50. Silinsh, E.; Capek, V., Organic Molecular Crystals: Interaction. *Localization, and Transport Phenomena, American Institute of Physics, New York* **1994**, 402.

51. Wurfel, P., The Chemical Potential of Radiation. *J. Phys. C: Solid State Phys.* **1982,** *15*, 3967.

52. Schick, K.; Daub, E.; Finkbeiner, S.; Würfel, P., Verification of a Generalized Planck Law for Luminescence Radiation from Silicon Solar Cells. *Appl. Phys. A* **1992,** *54*, 109-114.

53. Daub, E.; Würfel, P., Ultralow Values of the Absorption Coefficient of Si Obtained from Luminescence. *Phys. Rev. Lett.* **1995,** *74*, 1020.

54. Tebyetekerwa, M.; Zhang, J.; Liang, K.; Duong, T.; Neupane, G. P.; Zhang, L.; Liu, B.; Truong, T. N.; Basnet, R.; Qiao, X.; Yin, Z.; Lu, Y.; Macdonald, D.; Nguyen, H. T., Quantifying Quasi-Fermi Level Splitting and Mapping Its Heterogeneity in Atomically Thin Transition Metal Dichalcogenides. *Adv. Mater.* **2019,** *31*, e1900522.

55. El-Hajje, G.; Momblona, C.; Gil-Escrig, L.; Ávila, J.; Guillemot, T.; Guillemoles, J.-F.; Sessolo, M.; Bolink, H. J.; Lombez, L., Quantification of Spatial Inhomogeneity in Perovskite Solar Cells by Hyperspectral Luminescence Imaging. *Energy Environ. Sci.* **2016,** *9*, 2286-2294.

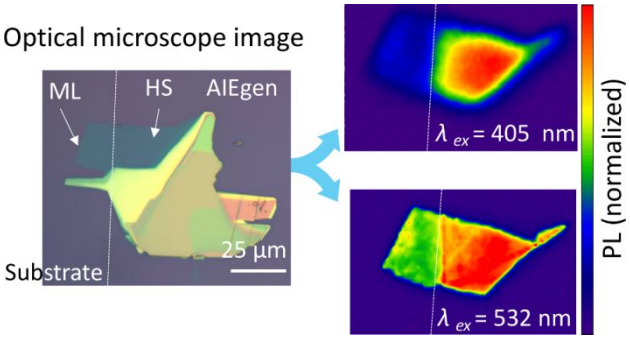

Table of Contents (TOC) graphic